

## Control of Tollmien–Schlichting waves using particle swarm optimization

Mohammadikalakoo, B.; Kotsonis, M.; Doan, N. A.K.

**DOI**

[10.1063/5.0243518](https://doi.org/10.1063/5.0243518)

**Publication date**

2024

**Document Version**

Final published version

**Published in**

Physics of Fluids

**Citation (APA)**

Mohammadikalakoo, B., Kotsonis, M., & Doan, N. A. K. (2024). Control of Tollmien–Schlichting waves using particle swarm optimization. *Physics of Fluids*, 36(12), Article 124130. <https://doi.org/10.1063/5.0243518>

**Important note**

To cite this publication, please use the final published version (if applicable).  
Please check the document version above.

**Copyright**





Other than for strictly personal use, it is not permitted to download, forward or distribute the text or part of it, without the consent of the author(s) and/or copyright holder(s), unless the work is under an open content license such as Creative Commons.

**Takedown policy**

Please contact us and provide details if you believe this document breaches copyrights.  
We will remove access to the work immediately and investigate your claim.

RESEARCH ARTICLE | DECEMBER 17 2024

## Control of Tollmien–Schlichting waves using particle swarm optimization

B. Mohammadikalakoo   ; M. Kotsonis  ; N. A. K. Doan 



*Physics of Fluids* 36, 124130 (2024)

<https://doi.org/10.1063/5.0243518>



### Articles You May Be Interested In

The sound field of a Tollmien–Schlichting wave

*Phys. Fluids* (March 1986)

Acoustic receptivity and transition modeling of Tollmien–Schlichting disturbances induced by distributed surface roughness

*Physics of Fluids* (April 2018)

On the interaction of Tollmien–Schlichting waves with a wall-embedded Helmholtz resonator

*Physics of Fluids* (March 2023)



Physics of Fluids

Special Topics Open  
for Submissions

[Learn More](#)

# Control of Tollmien–Schlichting waves using particle swarm optimization

Cite as: Phys. Fluids **36**, 124130 (2024); doi: [10.1063/5.0243518](https://doi.org/10.1063/5.0243518)

Submitted: 11 October 2024 · Accepted: 27 November 2024 ·

Published Online: 17 December 2024



View Online



Export Citation



CrossMark

B. Mohammadikalakoo,<sup>a)</sup>  M. Kotsonis,  and N. A. K. Doan 

## AFFILIATIONS

Department of Flow Physics and Technology, Faculty of Aerospace Engineering, Delft University of Technology, Kluyverweg 1, Delft 2629HS, The Netherlands

<sup>a)</sup> Author to whom correspondence should be addressed: [b.mohammadikalakoo@tudelft.nl](mailto:b.mohammadikalakoo@tudelft.nl)

## ABSTRACT

The implementation of the Particle Swarm Optimization (PSO) algorithm is investigated to optimize the active attenuation of Tollmien–Schlichting (TS) waves developing in a two-dimensional zero pressure gradient boundary layer. This is done numerically, where the PSO algorithm optimizes the characteristics of harmonic suction and blowing jets, in a feedforward control framework. The PSO-based controller selects and modifies the phase and amplitude of the jets to minimize the pressure fluctuation amplitude downstream of the actuator. To allow for efficient simulation, the 2-dimensional incompressible Navier–Stokes equations are expanded in a harmonic perturbation form and solved in linear and nonlinear variants using harmonic balancing. This study explores the performance of control in both linear and nonlinear development regimes of TS waves through control of single and multi-frequency ensembles of instabilities. Respectively, linear and nonlinear controller design approaches are employed. The findings reveal that the integration of PSO into the control design produces an effective suppression of TS waves through opposition control. The linearly designed controller effectively attenuates single and multi-frequency disturbances. However, when applied in regions of strong nonlinear interactions among instability modes, performance degradation is observed. On the contrary, the nonlinearly designed controller proves effective in mitigating nonlinear multi-frequency instabilities dominating the later stages of growth. A near-complete elimination of TS waves is achieved by accounting for nonlinear interactions among harmonic modes detected by an input sensor. This highlights the benefit of integrating the PSO algorithm in control of TS waves, particularly in the nonlinear growth regime, where classical control methods are generally ineffective.

© 2024 Author(s). All article content, except where otherwise noted, is licensed under a Creative Commons Attribution-NonCommercial 4.0 International (CC BY-NC) license (<https://creativecommons.org/licenses/by-nc/4.0/>). <https://doi.org/10.1063/5.0243518>

## I. INTRODUCTION

Tollmien–Schlichting (TS) waves are a prominent type of viscous instabilities, developing in two-dimensional boundary layers. They lead to transition from laminar to turbulent flow in low speed, low disturbance environments where pressure gradients are predominantly aligned with the flow direction.<sup>1</sup> As such, the suppression of TS waves amplitude during their early growth stages can delay transition, extend laminar flow, and reduce skin friction drag, making them an attractive target for both passive and Active Flow Control (AFC) methods.<sup>2–5</sup>

### A. State of the art

Numerous active control methods have been proposed and developed based on the wave superposition principle, admissible to TS waves' initial linear, two-dimensional wave-like development. The introduction of an opposing wave (of equal amplitude and opposite

phase) by actuators located typically near or at the wall is a common approach in the implementation of these techniques. Early experimental investigations have already proved the possibility of damping TS instabilities in their early linear growth stage.<sup>6,7</sup> These experiments were conducted in carefully managed flow environments, with single-frequency TS waves artificially introduced by means of vibrating ribbons. The developing monochromatic waves were superimposed by an opportune wall-mounted actuator operating with a properly adjusted amplitude and phase shift. Direct Numerical Simulations (DNSs) were also used to attenuate TS waves using a sensor-actuator arrangement on a flat plate demonstrating wave superposition through a spectral control approach.<sup>8</sup> Specifically, the spectral control approach was primarily focused on directly converting a sensor signal measured upstream into an actuating signal by adjusting amplification and phase shift. Their findings suggest that wave cancellation can be achieved for both small and large amplitude instabilities even without feedback. However, feedback is essential to fine-tune the control amplitude and

phase for precise wave cancelation, particularly in cases of multi-frequency wavetrains of instabilities.

Although the aforementioned early works treated the control of artificially introduced disturbances, the natural development of TS waves in realistic flow environments, such as those encountered in flight, brings forth considerable challenges. These primarily stem from the lack of *a priori* knowledge of incoming wave amplitude, frequency, or phase, necessitating, thus, the use of sensors in the so-called closed-loop approaches. The use of sensors further enables the implementation of adaptive control schemes and is able to fine-tune and optimize the control characteristics and performance in real time, even when operating conditions (e.g., Reynolds number, angle of attack, etc.) are changing. Model-based<sup>9,10</sup> and model-free<sup>11–15</sup> control strategies are two common methods for the control of convective instabilities depending on whether a model that describes the flow problem is provided.

A model-based approach operates under the assumption that the controller possesses a comprehensive understanding of the flow problem, largely relying on the principles of linear system theory. Such model-based approaches have found widespread application in the control of convective instabilities within two-dimensional boundary layer flows.<sup>9,10,16,17</sup> In all model-based control strategies, the necessity of an accurate flow model is a limitation that becomes critical in realistic flow conditions, where a spatially and temporally accurate flow model is usually unavailable. Furthermore, the performance of the control will decline even with a presumed model if the global flow conditions change significantly beyond what the model can predict. Model-free techniques, which rely on system identification methods, can address this issue and have demonstrated success in flow control applications.<sup>14</sup>

Adaptive control is among the most widely utilized model-free control strategies for convective instabilities, capable of real-time optimization of control performance. Early investigations into adaptive control of convective instabilities on flat plates and axisymmetric bodies<sup>18–20</sup> as well as on an unswept wing<sup>21–23</sup> demonstrated successful cancelation of naturally occurring TS instabilities. Later, attention was drawn to adaptive filter-based controllers due to promising experimental results.<sup>11</sup> Specifically, successful suppression of both artificially induced and naturally occurring TS waves was reported, with a reduction in amplitude over 94% by employing an adaptive Filtered-x Least Mean Square-based controller. Research on filter-based adaptive control techniques for convective instabilities has continued, spanning numerical,<sup>4</sup> in-flight,<sup>14</sup> and experimental testing.<sup>13</sup>

Taking into account the investigations mentioned earlier, the control of TS waves in realistic flow conditions remains a challenging task for classical model-based or model-free control strategies. The challenge largely pivots on the nondeterministic, yet bounded spectrum of naturally occurring TS waves.<sup>10</sup> In addition, current model-based and model-free approaches rely solely on the principles of linear wave superposition. This inherently restricts the practical “window of opportunity” for control to a narrow spatiotemporal regime where boundary layer instabilities attain sufficient amplitude for the detection by sensors, yet remain sufficiently weak to admit linear development and dynamics. To extend this operational window of control and accommodate inherent limitations in sensitivity and cost of sensors, it is necessary to explore flow control techniques, which are able to effectively suppress naturally occurring TS waves in their highly nonlinear stage of development.

Artificial Intelligence (AI) techniques capable of handling high nonlinearity and dimensionality could effectively address the need for advanced control laws to suppress TS waves.<sup>24</sup> The application of these algorithms in fluid dynamics has led to significant advancements, particularly in resolving partial differential equations,<sup>25</sup> turbulence modeling,<sup>26</sup> aerodynamic shape optimization,<sup>27,28</sup> flowfield reconstruction from limited measurement data,<sup>29</sup> and active flow control in nominal laminar<sup>30–36</sup> and turbulent<sup>37,38</sup> regimes.

Among the flurry of artificial intelligence based methods, the Particle Swarm Optimization (PSO) algorithm is particularly noted for its ease of implementation as it operates on principles of swarm intelligence, first introduced by Ref. 39. PSO has found extensive use across diverse domains, including machine learning and adaptive control.<sup>40–42</sup> Inherently, PSO is a population-based optimization tool that can be easily implemented and applied to solve various function optimization problems or problems that can be transformed into function optimization problems. The main advantage of this approach resides in its rapid convergence compared to other global optimization algorithms like Genetic Algorithms (GA) and Simulated Annealing.<sup>43</sup> Another advantage of PSO is its ability to handle non-differentiable problems, as it does not rely on the gradient of the problem in its optimization process. Furthermore, the method is compatible with distributed implementation due to the unique combination of individual and social components.<sup>44</sup> Therefore, PSO can be parallelized and distributed across multiple computing nodes to accelerate the optimization process. This distributed approach makes PSO an efficient algorithm for large-scale optimization problems.

The application of the PSO algorithm in fluid dynamics is limited to a few studies exploring shape optimization<sup>45</sup> and biomechanics applications.<sup>46</sup> However, its rapid convergence in optimization problems with high-dimensional exploration space, coupled with its capacity to optimize nonlinear problems through swarm intelligence, renders it as an ideal candidate for driving AFC systems aimed at controlling convective instabilities.

## B. Present work

In the current work, the performance of a model-free PSO-based strategy in controlling TS waves is evaluated in two phases. First, optimum control parameters are identified toward suppressing TS waves in the linear development stage. Second, control is extended to a highly nonlinear stage of development with the primary objective of overcoming limitations of classic control strategies, which confined control of TS waves exclusively within their linear growth regime. Enabling control in the nonlinear growth regime of TS waves enhances the ability to detect disturbances by sensors and extends the temporal and spatial control horizon. This adds flexibility for actuator/sensor positioning and type utilized in future control systems.

This study employs a closed-loop feedforward control framework comprised of wall-mounted harmonic suction and blowing jets as actuators, along with the PSO algorithm for determining the optimal amplitude, and phase of these jets based on sensor feedback relies on measuring the wall pressure perturbations. Linear (superposition) and nonlinear approaches are employed for designing the controller, followed by a comparative analysis of control strategy performance between the two approaches. Here, it must be noted that the objective of this work is not to outperform existing classical control techniques but rather to provide a proof-of-concept for a PSO-based controller in

these flows. The main ambition of this work is to explore the potential of PSO-based strategies in controlling TS waves in the nonlinear growth regime. Therefore, comparing controller performance with available classical control techniques falls outside the scope of this study.

The work is organized as follows. Section II presents the employed methodology, outlining the flow problem, numerical solver, and control system. Section III evaluates and discusses the controller performance for control cases ranging from linear to highly nonlinear. Finally, insights gained from this study are summarized in Sec. IV.

II. METHODOLOGY

This section presents the flow problem, numerical method, and control technique utilized for simulating and controlling TS waves in an incompressible 2D laminar boundary layer. A Harmonic Navier–Stokes (HNS) methodology is utilized in both linear and nonlinear formulations, as detailed in Ref. 47. The decision to use the HNS approach is motivated by its capability to exploit the temporal periodicity of TS waves and model their evolution in the frequency domain. This greatly increases computational efficiency in relation to a more classical time-dependent solution of the Navier–Stokes equations.

A. Flow problem

For the entirety of this work, the development and control of TS waves in a flat plate (i.e., zero pressure gradient) boundary layer flow is considered. Figure 1 displays the physical and computational domains as well as a conceptual representation of the flow control system. The spatial dimensions are globally non-dimensionalized using the Blasius length scale defined at the inflow of the simulation domain ( $x_0$ ), denoted as  $\delta_0 = \sqrt{\frac{x_0 \nu_0}{U_\infty}} = 6.075 \times 10^{-4} \text{m}$ .

The gray region in Fig. 1 represents the computational domain  $\Omega = [x_0 = 400, L_x = 2480] \times [0, L_y = 82]$ . The virtual origin for the laminar boundary layer is located at ( $x = 0$ ), and a self-similar Blasius boundary layer at the inflow of the computational domain is assumed. The freestream streamwise velocity  $U_\infty$  is assumed constant (i.e., zero pressure gradient) at a value of  $10 \frac{m}{s}$ , corresponding to Reynolds number  $Re_0 = \frac{U_\infty \delta_0}{\nu_0} = 400$ , with kinematic viscosity  $\nu_0 = 1.511 \times 10^{-5} \frac{m^2}{s}$ .

The spectral analysis of the TS wave enables the representation of these convective instabilities as individual harmonics with a modal notation of ( $m, n$ ) developing in a precalculated steady laminar base flow. The higher harmonic modes are defined based on the fundamental spanwise wavenumber ( $\beta_1$ ) and angular frequency ( $\omega_1$ ), where  $\omega_m = m\omega_1$  and  $\beta_n = n\beta_1$ . More details on the numerical discretization are presented in Sec. II B describing the Harmonic Navier–Stokes framework. To enforce the inflow instability, TS wave modes (depending on test cases—Sec. II A 1) are imposed at the inflow as a solution to the local eigenvalue stability problem. For the entirety of this work, purely two-dimensional TS waves are considered (i.e.,  $\beta_n = 0$ ). The normalized frequency of each mode, denoted as  $F$ , is defined as

$$F = \frac{\omega_0}{Re_0} \times 10^6, \quad \omega_0 = \frac{2\pi\delta_0 f}{U_\infty}, \quad (1)$$

where  $\omega_0$  in Eq. (1) refers to the local non-dimensional frequency of the mode, while  $F$  is the non-dimensional frequency based on the inflow Reynolds number.  $f$  is the physical dimensional frequency of the mode. Three frequencies ( $F_1 = 28, F_2 = 57, F_3 = 86$ ) are considered in this study. The corresponding instability modes are marked on the stability diagram of this flow as predicted by Linear Stability Theory, as shown in Fig. 2.

As evident in Fig. 2, for the chosen frequencies, the corresponding TS wave modes are introduced at the domain inflow upstream of their respective neutral points. This facilitates the initial damping of any transient behavior resulting from the inlet conditions as well as provides a more realistic representation of natural flow conditions.<sup>4</sup> Additionally, the stability diagram in Fig. 2 reveals that the range of effective frequencies for the studied Reynolds number is narrow. Frequencies that are too low result in no growth of TS waves, while frequencies that are too high cause early stabilization of TS waves before reaching the actuator, especially for the downstream control scenario. These constraints ultimately guide the selection of these three frequencies ( $F_1 = 28, F_2 = 57, F_3 = 86$ ).

The amplitude of the TS wave modes at the inflows is defined by a peak streamwise perturbation velocity and set to a root mean square

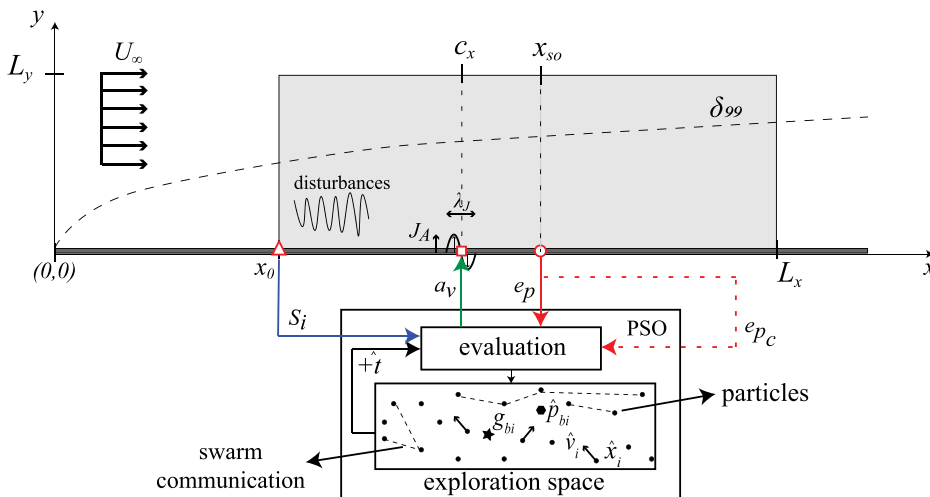
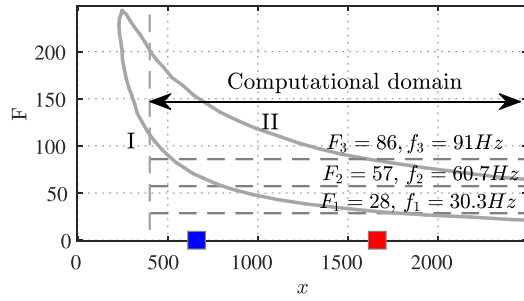


FIG. 1. Schematic view of the PSO-based control system for the suppression of TS waves in a 2-D flat plate boundary layer. Width of actuator:  $\lambda_A$ . The actuator's center is located at ( $C_x, 0$ ). The control inputs ( $S_i, e_{pc}, e_p$ ) and outputs ( $a_v$ ) are reviewed in Sec. II C. The terms related to the PSO algorithm ( $\hat{p}_{bi}, g_{bi}, \hat{x}_i, \hat{v}_i$  and  $\hat{v}_i$ ) are defined in Sec. II C 1.

30 December 2024 07:48:43



**FIG. 2.** Stability diagram of the considered flow based on Linear Stability Theory analysis. The solid gray line is the neutral curve. The location of the actuator is presented with blue and red square markers for upstream ( $C_x = 660$ ) and downstream ( $C_x = 1653$ ) control cases, respectively.

value of 0.25% of the freestream velocity, as described in Ref. 48, except for the final test case, which will be discussed in Sec. II A 1.

Harmonic suction and blowing jets used for the control of TS waves are defined by boundary conditions applied at the wall. The spatial distribution of blowing/suction velocity is defined through a sinusoidal function ( $J_A \cdot \sin(2\pi x_s) \cdot e^{i(t/\phi)}$ ).  $J_A$  and  $J_\phi$  denote the actuation amplitude and phase, respectively.  $x_s \in [0, 1]$  is the local normalized streamwise coordinate based on actuator width ( $\lambda_j$ ). The location and spatial wavelength (width) of the harmonic suction and blowing jets are determined based on a parametric study.

In the control system, a reference signal and an error signal are utilized, both derived from pressure values measured at the wall. The reference signal is acquired directly at the domain inflow ( $x_0 = 400$ ) to detect incoming instabilities. The choice of such an upstream position for the reference signal sensor was made to ensure minimal upstream influence from the actuator. Similarly, the error sensor is positioned downstream of the actuator at a distance equal to twice the longest investigated TS wavelength ( $X_{s0} = 1782$ ). This allows any spatial transients in the controlled instabilities to decay prior to reaching the error monitoring location.

**1. Test cases**

Four TS wave cases (A – D) are considered in this study and presented in Table I. Case A describes the linear development of a

single-frequency ( $F = 86$ ) disturbance introduced at the domain inflow. The control system is developed and tested in two distinct configurations, respectively, utilizing an upstream-located actuator ( $C_x = 660$ ) and a downstream-located actuator ( $C_x = 1653$ ). This variation in actuator location allows for the assessment of the control system’s performance in a scenario where the actuator is required to suppress a highly amplified TS wave. Case B is designed as a nonlinear extension of case A. Through the activation of nonlinear interactions within the HNS framework, the primary mode ( $F = 86$ ) introduced at the inflow naturally generates higher harmonics downstream, as illustrated in Ref. 49. In addition to the appearance of higher harmonics, nonlinear interactions also contribute to a time-invariant modification of the mean flow, often represented as mode (0, 0) and referred to as Mean Flow Distortion (MFD).

Cases C and D explore a fully nonlinear development of ensembles of TS waves introduced at the inflow at frequencies  $F = 86, 57,$  and  $28$ . In these cases, all three harmonics have a finite initial amplitude imposed at the inflow, and only the mean flow distortion is naturally generated, as illustrated in Fig. 3. This ensemble gives rise to intensified nonlinear interactions, thereby increasing the complexity of the flow control task. The initial amplitude of the first three modes in case C is set as equal to 0.25%. For case D, the initial amplitude of the first two modes ( $F = 28$  and  $57$ ) is increased to 0.5%, while the third mode ( $F = 86$ ) is kept at 0.25%. This adjustment in case D is based on a preliminary study, indicating that the increase in the initial amplitude of the higher harmonics should be carefully selected due to the constraints of the HNS solver. Excessive amplitude at the inflow could cause solver divergence by laminar breakdown downstream, which deviates from the core assumptions underlying the used solver.

The various harmonics illustrated in Fig. 3 play distinct roles in shaping the TS wave. In case C, mode (2, 0) is notably stronger, exhibiting a peak amplitude positioned toward the domain’s downstream end. This higher influence of mode (2, 0) underscores the heightened nonlinear effects present in case C. The initial amplitude of the TS wave’s modes can significantly affect the degree of dominance of nonlinear interactions. For instance, case D reveals distinct nonlinear harmonics compared to the other cases, as depicted in Fig. 3. The dominant mode is no longer mode (3, 0), and the amplitudes of the harmonics are pronounced. These four cases cover a wide range of linear to highly nonlinear dynamics of TS wave development, in which the PSO control strategy needs to operate.

**TABLE I.** Summary of test cases explored in the present work.  $F_i$  and  $F_c$  refer to the frequency of introduced modes at the inflow and the frequency of controlled modes, respectively.  $S_i$  indicates the initial root mean square amplitude for each mode. The location of the actuator is defined with  $C_x$ .

Cases	Simulation	Control design	$F_i$ ( $S_i$ in RMS)	$F_c$	$C_x$
A1	Linear	Linear	$F_1 = 86$ (0.25%)	$F_1 = 86$	660
A2					1653
B1	Nonlinear	Linear	$F_1 = 86$ (0.25%)	$F_{1-3}=28, 57, 86$	660
B2					1653
C1	Nonlinear	Linear	$F_{1-3}=28, 57, 86$ (0.25%)	$F_{1-3}=28, 57, 86$	660
C2					1653
D1	Nonlinear	Linear	$F_{1-3} = 28, 57$ (0.5%), $86$ (0.25%)	$F_{1-3}=28, 57, 86$	660
D2					1653
D2n	Nonlinear	Nonlinear	$F_{1-3} = 28, 57$ (0.5%), $86$ (0.25%)	$F_{1-3}=28, 57, 86$	1653

30 December 2024 07:48:43

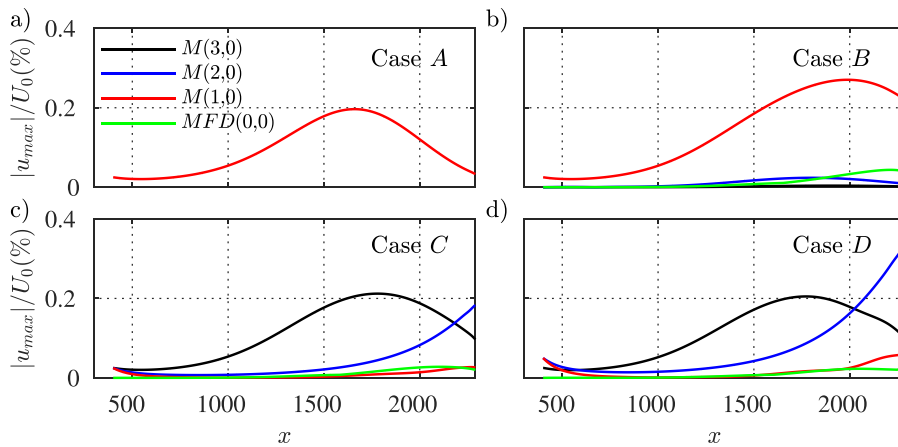


**FIG. 3.** Normalized amplitude evolution based on maximum modal streamwise velocity for test cases A–D (uncontrolled).  $M(m, n)$  is the modal notation, and MFD represents the modification of the base flow by nonlinear mode interactions.

## B. Harmonic Navier-Stokes framework

To effectively model the development of Tollmien–Schlichting waves in both linear and nonlinear growth scenarios, the incompressible Navier–Stokes equations are considered in perturbed form. The instantaneous flow is decomposed as the summation of a steady base flow,  $Q(x, y, z) = [U, V, W, P]$ , and a fluctuating flow,  $q'(x, y, z, t) = [u', v', w', p']$ .

The steady base flow is extracted as a solution of the incompressible boundary layer equations. The boundary layer equations are solved in a marching scheme and initiated at the inflow with a precalculated boundary layer profile derived from the local solution of the Falkner–Skan–Cooke equations at an equivalent Hartree parameter to the local pressure gradient. Dirichlet boundary conditions for pressure and Neumann boundary conditions for velocity are applied at the free-stream. The no-slip condition is set for the wall. The steady base flow solution is calculated once prior to the HNS simulations and is used identically in all test cases reported in this work.

For the simulation of the fluctuating flow, a periodic temporal and spanwise spatial harmonic behavior is assumed through a double Fourier ansatz, Eq. (2). This assumption greatly reduces the complexity of the Navier–Stokes equations by removing the need to discretize two primary dimensions (i.e., time and spanwise space), effectively reducing the physical problem to a two-dimensional state-space,

$$q'(x, y, z, t) = \sum_{m=-M}^M \sum_{n=-N}^N \hat{q}_{m,n}(x, y) e^{i(\beta_n z - \omega_m t)}. \quad (2)$$

Specifically, the perturbation is harmonically expanded in both the spanwise ( $z$ ) direction and time ( $t$ ). The vector  $\hat{q}$  describes the Fourier modal shape of the perturbation in the  $x - y$  plane, while  $\omega_m$  is the modal angular frequency. The parameter  $\beta_n$  denotes the spanwise modal wavenumber and, in general form, is a non-dimensional complex coefficient describing the growth (or decay) and periodicity of the perturbations in the  $z$ -direction. Notably, in this investigation,  $\beta_n$  is assumed to be purely real, given that the base flow is strictly invariant in the  $z$ -direction. Consequently, the perturbation does not exhibit growth in the spanwise direction.

The angular frequency and spanwise wavenumber of higher harmonic modes is defined based on the fundamental wave

specification  $(\omega_1, \beta_1)$  with modal notation  $(m, n)$ , where  $\omega_m = m\omega_1$  and  $\beta_n = n\beta_1$ , as discussed earlier. In addition,  $M$  and  $N$  indicate the truncation limit of modes. In the present work,  $M = 3$  and  $N = 0$ . Specifically, the truncation of the temporal harmonic (i.e.,  $M$ ) to the first 3 harmonics and MFD is confirmed to capture more than 92% of the total kinetic perturbation energy.<sup>47</sup> This is sufficient to demonstrate the proof of concept of the controller while avoiding the additional computational cost of adding more harmonic modes.

Upon substituting Eq. (2) into the general Navier–Stokes equations and neglecting the exponential terms associated with the harmonic perturbation, the Harmonic Navier–Stokes equations are produced. These equations exhibit inherent nonlinearity, but they can be linearized if deemed necessary, yielding both the Nonlinear Harmonic Navier–Stokes (NLHNS) and Linear Harmonic Navier–Stokes (LHNS) equations. In the present work, the in-house Delft Harmonic Navier–Stokes Solver (DeHNSSo) is utilized for the solution of the HNS system. For a comprehensive description of the formulation, discretization, and implementation of DeHNSSo, interested readers are referred to Ref. 47.

## 1. Numerical setup

Both base flow and perturbation fields are solved on a uniform grid in the streamwise direction ( $x$ ). Two different resolutions are used for the boundary layer equations solution (i.e., base flow) and the HNS system (i.e., perturbations). For the boundary layer solution, a grid with 5000 uniform grid points is used in the  $x$ -direction, while for the HNS solution, 1200 uniform grid points are used. This grid density ensures at least 30 grid points per TS wavelength for the shortest wavelength case. In the HNS framework, first and second streamwise derivatives are approximated with a fourth-order central finite difference scheme.

In the  $y$ -direction, both boundary layer and HNS equations are discretized using a spectral collocation method employing the Chebyshev polynomial basis function. The spatial mapping proposed in Ref. 50 is utilized for providing improved resolution in the near-wall region of the boundary layer. The non-uniform grid in the  $y$ -direction comprises 100 collocation points, arranged in such a way that half of

the points are located below  $y/H = 0.1$ , where  $H$  represents the height of the domain.

The HNS framework requires the definition of appropriate boundary conditions. At the inflow, an eigensolution to the linearized stability equations is used to initiate the selected instability modes. At the outflow, a damping buffer region is used to prevent nonphysical reflections resulting from the domain truncation. The damping function within the buffer region follows a smooth hyperbolic tangent shape and is applied directly to the perturbation terms.<sup>8,51</sup> At the wall, the no-slip condition is enforced for all perturbation modes. Similar conditions are applied at the freestream with the exception of the MFD mode, which is allowed to grow by expulsion of wall-normal velocity through the top boundary.

The nonlinear discretized HNS equations are decomposed into a system of mode-specific equations through the use of the harmonic balancing procedure.<sup>52</sup> Using this method, each mode is solved sequentially, while nonlinear interactions are kept as forcing terms and iteratively updated. Eventually, for each mode, the resulting system of equations is formulated in the matrix form, as shown in the following equation:

$$[A_{m,n}]\hat{q}_{m,n} + [B_{m,n}]\frac{\partial \hat{q}_{m,n}}{\partial x} + [F_{m,n}]\frac{\partial^2 \hat{q}_{m,n}}{\partial x^2} = r_{m,n}. \quad (3)$$

It is important to note that Eq. (3) pertains to the nonlinear formulation for mode  $(m, n)$ , where all nonlinear forcing terms are incorporated on the right-hand side  $r_{(m,n)}$  for each mode. Matrices  $A$ ,  $B$ , and  $F$  encompass the base flow data and the characteristics of each mode. Upon solving this system, one obtains the desired perturbation velocity and pressure for each mode. The explicit form of the matrices and equations of HNS can be found in Ref. 47.

The final resolution of numerical grids and dimensions of the computational domain including domain height and collocation median point are chosen based on a preliminary convergence study for the LHNS solver. Interested readers are referred to Ref. 47 for a detailed grid convergence study of DeHNSSo.

### C. Control framework

The closed-loop feedforward control framework in this study consists of harmonic wall-normal suction and blowing jets used as actuators, and the PSO algorithm that selects the optimum amplitude and phase of the jets. The maximum amplitude of the TS wave's streamwise velocity and wall pressure perturbations is measured to provide the necessary information to the controller.

In the implemented control system (Fig. 1), the PSO algorithm receives the reference signal ( $S_i$ ) measured at the computational domain inflow by the pressure sensor from which it extracts the TS wave's characteristics such as frequency, phase, and amplitude. A baseline error signal ( $e_{p_s}$ ) observed during the actuator inactivity represents the baseline state. The error signal ( $e_p$ ) emerges when the control system is active, monitoring instabilities following actuation.

The core objective of the PSO algorithm is to adjust the actuator's amplitude and relative phase ( $a_v$ ) to suppress the amplitude of the TS wave. This optimization process hinges on maximizing a predefined cost function established within the controller's evaluation unit. The PSO algorithm and its mathematical operations are briefly described in the following sections.

### 1. PSO algorithm

The PSO algorithm finds an optimal solution through an iterative improvement of candidate solutions using a measure of quality (i.e., a reward or loss function). Here, without loss of generality, the maximization of a problem-dependent cost function  $C$  is considered. Initially, a population of particles, each representing a candidate solution, is randomly initialized. In the present work, one such PSO particle corresponds to one distinct HNS simulation, featuring a set combination of actuator parameters such as amplitude, phase, etc. Each particle has a so-called "position" that represents a solution or candidate point within the search space and a so-called "velocity" (step size) that indicates the rate at which the position changes within that search space between two successive iterations of the PSO algorithm. At the  $\hat{t}$  th iteration, the  $N_p$  particle's positions and velocities in the  $d$ -dimensional search space are defined by two vectors as  $\hat{x}_i(\hat{t}) \in \mathbb{R}^d$  and  $\hat{v}_i(\hat{t}) \in \mathbb{R}^d$ , respectively. At iteration  $\hat{t} + 1$ , the position and velocity of the  $i$ th particle are updated based on its individual personal best position,  $\hat{p}_{b,i}(\hat{t})$ , and the global best position,  $g_b(\hat{t})$ , according to Eqs. (4) and (5). Variables in the PSO algorithm are denoted with a hat (e.g.,  $\hat{t}$ ) to distinguish them from similarly defined variables in other sections,

$$\hat{v}_i(\hat{t} + 1) = \hat{\omega}\hat{v}_i(\hat{t}) + c_1r_1(\hat{p}_{b,i}(\hat{t}) - \hat{x}_i(\hat{t})) + c_2r_2(g_b(\hat{t}) - \hat{x}_i(\hat{t})), \quad (4)$$

$$\hat{x}_i(\hat{t} + 1) = \hat{x}_i(\hat{t}) + \hat{v}_i(\hat{t} + 1). \quad (5)$$

The individual personal best position of the  $i$ th particle at iteration  $\hat{t}$  corresponds to the best position (according to the cost function  $C$ ) encountered by the  $i$ th particle up to iteration  $\hat{t}$  and is defined as

$$\hat{p}_{b,i}(\hat{t}) = \underset{\hat{x}_i}{\operatorname{argmax}}\{C(\hat{x}_i(\hat{n})), \hat{n} = 0, \dots, \hat{t}\}. \quad (6)$$

The global best position at iteration  $\hat{t}$ ,  $g_b(\hat{t})$ , then corresponds to the best  $\hat{p}_{b,i}(\hat{t})$  among all the  $N_p$  particles in the swarm and is defined as

$$g_b(\hat{t}) = \underset{\hat{p}_{b,i}}{\operatorname{argmax}}\{C(\hat{p}_{b,i}(\hat{t})), i = 1, \dots, N_p\}. \quad (7)$$

After computing the new positions at iteration  $\hat{t} + 1$ , using Eq. (5), the updated personal best of each particle ( $\hat{p}_{b,i}$ ) and global best ( $g_b$ ) of the population are obtained according to Eqs. (6) and (7).

In Eq. (4), the PSO algorithm includes some hyperparameters:  $\hat{\omega}$  as the inertia weight coefficient to control the previous velocity contribution in the updated velocity, and  $c_1$  and  $c_2$  as the personal learning and global learning factors, respectively. The influence of the particle self-exploration is determined by  $c_1$ , while  $c_2$  indicates the influence of the global best position in the entire swarm. Additionally,  $r_1$  and  $r_2$  are random variables sampled from uniform distributions between zero and one at each iteration, which are employed to preserve the population's variety.

These update and evaluation steps are iterated until convergence of the solution is achieved. The PSO algorithm, as a metaheuristic method, does not guarantee the discovery of the global optimum of an optimization problem. However, by using specific sets of hyperparameters, PSO can converge to one of the best local optimum regions within the exploration area.<sup>53</sup> The strategy makes few or no assumptions about the optimization problem and does not require



incorporating the physics of the problem into the algorithm. This characteristic makes it a versatile optimization method suitable for a wide range of problems, enabling it to explore a large search space in a stochastic manner.

It is worth noting that changing the hyperparameters of the PSO algorithm can affect the convergence rate of the algorithm. However, the initial random selection of the PSO is unlikely to significantly impact the convergence behavior of the algorithm, although it may produce minor differences in the final optimum point.

### 2. PSO-based TS wave control

For the PSO-based controller used in the present study, the set of hyperparameters resulting from a preliminary parametric study is specified as  $(\hat{\omega}, c_1, c_2) = (0.9, 0.9, 1.2)$ . The  $(\hat{\omega} = 0.9)$  follows the general suggestion of inertia weight in the  $[0.8, 1.2]$  range, which enhances the chance of finding the global optimum within a moderate number of iterations.<sup>54</sup> Furthermore, these hyperparameters are selected within the algorithm stability region,  $-1 < \hat{\omega} < 1$ ,  $0 < c_1 + c_2 < 4(1 + \hat{\omega})$ , to guarantee the convergence of the algorithm.<sup>55</sup> The higher value of the global learning rate compared to the local learning rate helps in situations where individual particles might be stuck in local optima, as it encourages the particle movement to rely more on the swarm's collective knowledge.

The exploration space parameters are also provided in Table II. The choice regarding the number of iterations and particles within each iteration was made to balance the exploration and exploitation phases of the algorithm. A higher number of particles means more exploration necessitating a longer convergence time. This is a limiting factor considering the controller's practical applicability and the available computational resources for this study.

The PSO algorithm seeks to maximize the cost function,  $C$ , defined in Eq. (8). This cost functional has two terms,  $\Delta P_{err,r}$  and  $E'$ , which represent the reduction in pressure perturbation at the error sensor location relative to the uncontrolled case and a relative energy expenditure term, respectively, with  $w_e$  being a weighting term between these two terms,

$$C = \Delta P_{err,r} - w_e E'. \tag{8}$$

Specifically,  $\Delta P_{err,r}$  represents the attenuation of TS wave defined here as the relative difference in the pressure perturbation measured by the error sensor between scenarios with  $(e_p)$  and without active

flow control  $(e_{p_c})$ , the latter denoted as the “baseline case.” It is, therefore, defined as

$$\Delta P_{err,r} = \frac{e_{p_c} - e_p}{e_{p_c}}, \tag{9}$$

where  $E'$  corresponds to the ratio between the mass flow rate of the harmonic suction and blowing jets,  $E_j$ , and the maximum achievable mass flow rate constrained by the exploration space of the PSO,  $E_{j_{max}}$ , which is used as a proxy for the energy expenditure of the actuator. It is defined as

$$E' = \left( \frac{E_j}{E_{j_{max}}} \right), \tag{10}$$

where  $E_j$  and  $E_{j_{max}}$  are defined in Eqs. (11) and (12), respectively,

$$E_j = \int_0^{L_x} |J_A \cdot \sin(2\pi x)| dx, \tag{11}$$

$$E_{j_{max}} = \int_0^{L_x} |J_{A_{max}} \cdot \sin(2\pi x)| dx. \tag{12}$$

In the above,  $J_A$  corresponds to a user-defined term that the PSO algorithm will have to optimize. The energy-related penalty in Eq. (8) carries a weight of  $w_e$ . A larger weight motivates the PSO algorithm to prioritize lower actuation amplitudes at the expense of maximum wave suppression. A weight of 10% was found as a reasonable trade-off, based on a preliminary parametric study.

In addition to the cost function defined earlier, in the following discussion, the attenuation of the pressure perturbation will also be discussed in terms of dB reduction, defined as follows:

$$\Delta P_{err,dB} = 10 \cdot \log_{10} \left( \frac{e_p}{e_{p_c}} \right). \tag{13}$$

To ensure compliance with realistic and realizable actuators necessary for the eventual deployment of the control framework to an experimental setting, the actuation amplitude and phase are manually bounded in the PSO algorithm, specifically defined by lower and upper boundaries in Table II. The actuator phase shift with respect to the reference signal,  $S_i[\phi]$ , is  $\pm\pi$ , while the actuation amplitude is free to change from zero to the amplitude of the reference signal,  $S_i[A]$ . This provides a large exploration space for the algorithm. However, the amplitude and phase selection for the actuator are not solely constrained by the upper and lower bounds since the cost function takes into consideration the energy expenditure of the jets as an extra limiting factor.

### 3. Control design approach

For the control of the nonlinear cases ( $B - D$ ), each harmonic mode of the TS wave is individually controlled. This approach is necessitated by the nature of the disturbance signal, which is treated as a summation of harmonics. The control of each mode is then performed similarly to case A, where a single-frequency disturbance matching the mode's frequency is introduced at the inflow, and a corresponding control action is found for each mode. Finally, the action of the actuator is superimposed by a summation of the control actions for each individual mode. This approach is referred to as the “superposition method.”

**TABLE II.** PSO algorithm parameters.  $N_p$  represents the number of particles and  $d$  refers to the number of parameters to be controlled including the amplitude and phase of the jets.  $t$  is the maximum number of optimization iterations.

Parameters	Value
$N_p$	20
$d$	2
$t$	1000
$J_A \in$	$[0, S_i[A]]$
$J_\phi \in$	$[S_i[\phi] - \pi, S_i[\phi] + \pi]$

Through the superposition method, it becomes feasible to apply an identical control strategy as applied to the case *A* to nonlinear scenarios while keeping computational expenses at a minimum. The main potential lies in developing a lookup table comprising controllers for the linear modes, which can then be utilized to control varied combinations of these harmonics in various nonlinear scenarios. The effectiveness of this approach in three different test cases (*B* – *D*) is evaluated in Sec. III and compared with the nonlinear design approach for case *D* in Sec. III E. In the nonlinear design of the controller, the control system is applied directly to the nonlinear cases instead of depending on the superposition technique.

The nonlinearly designed controller incurs substantial computational expenses, primarily driven by the computational cost of the nonlinear harmonic Navier–Stokes equations in comparison to their linear counterparts. This complexity arises from an iterative method employed for nonlinear forcing terms within the NLHNS framework. These nonlinear forcing terms are retained as a lagged source term on the right-hand side of Eq. (3) and are updated iteratively per mode.<sup>47</sup> The computational outlay associated with nonlinear scenarios, even when considering merely three principal harmonics, could be as much as 30 times greater than that in linear scenarios.

### III. RESULTS

The controller performance in several test cases ranging from linearly developing single-frequency TS waves to nonlinearly developing multi-frequency control cases is explored in this study and presented in the following four control cases (i.e., *A* – *D*). The section proceeds with discussions concerning the control strategy, along with a comparative analysis of the controller performance across various test cases. Finally, the discussion concludes with a comparison between linearly designed (i.e., superposition method, case *D2*) and nonlinearly designed (i.e., case *D2n*) controllers.

#### A. Control case A: Linear single-frequency control

Control cases *A1* and *A2*, respectively, employing upstream ( $C_x = 660$ ) and downstream ( $C_x = 1653$ ) actuators are explored in the context of linearly developing single-frequency ( $F = 86$ ) TS waves introduced at the domain inflow. The arrangement of the actuator and sensors is depicted in Fig. 1 and Table I.

Figure 4 illustrates the evolution of key performance characteristics of the control framework as a function of training episodes, encompassing concurrent exploration and evaluation phases. Specifically, the PSO algorithm assesses the action's performance after every 20 episodes (actions) using exploration data to determine the subsequent 20 actions. The optimal action of the PSO-based controller is denoted by a red star in Fig. 4.

As demonstrated in Fig. 4, the control strategy effectively suppresses the amplitude of the instability, demonstrating noticeable attenuation before reaching 100 episodes. However, the controller's full convergence requires a more extended period, ultimately converging after 580 episodes. As will be shown in the following cases, control performance convergence varies greatly as a function of the active instability modes and linearity of dynamics. The convergence is generally attained within 400 – 800 episodes, depending on the control case. In an equivalent real-time framework, this corresponds to approximately 8 – 16 s, equivalent to 130 – 260 convective time units, calculated based on the Blasius length scale at the inflow.

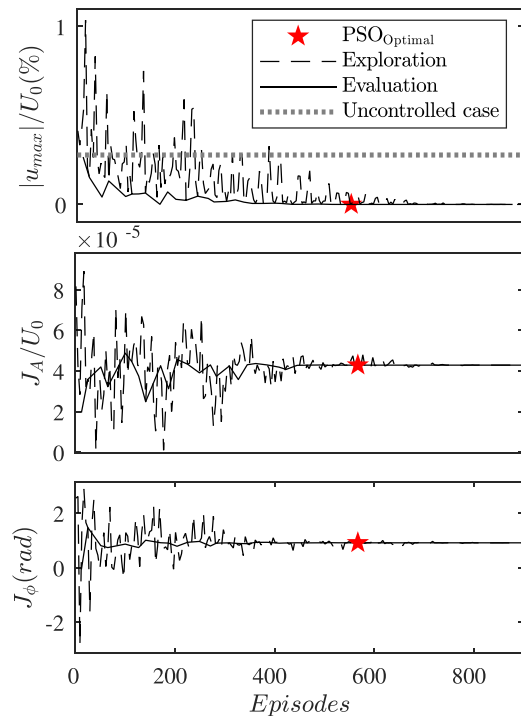


FIG. 4. Illustration of controller performance convergence for case A1.  $|u_{max}|$  is the maximum amplitude of streamwise disturbance velocity, and  $J_A$  is the actuation amplitude.  $J_\phi$  signifies the relative phase of the actuator blowing action with respect to the TS wave wall-normal velocity at the input sensor.

The normalized maximum streamwise velocity shown in Fig. 5 highlights that the controller reduces the instability amplitude, achieving a decrease by an order of magnitude for both cases *A1* and *A2*. However, downstream of the actuator's location, the boundary layer resides within the unstable region for the investigated mode, causing the remaining disturbance to rapidly amplify once again. This phenomenon underscores the significance of employing multiple consecutive actuators in real-world applications to ensure a sustainable and significant delay of transition.<sup>4</sup>

Upon comparing the suppression of TS waves in cases *A1* and *A2* in Fig. 5, it becomes evident that the upstream actuator is more effective in locally suppressing TS waves. Nevertheless, the growth of controlled instabilities following the upstream actuation results in nearly identical suppression values as those achieved by the downstream actuator, as presented in Table III. This is largely expected due to the purely linear regime of case *A*. The attenuation of the signal in Table III is calculated based on the superposition of all modes, both in controlled and uncontrolled cases, measured at the error sensor location ( $X_{so} = 1782$ ).

#### B. Control case B: Weakly nonlinear single-frequency control

Case *B* explores the control of a nonlinearly developing TS wave. In this instance, a single-frequency disturbance ( $F = 86$ ) is introduced at the inflow, mirroring the approach employed in case *A*. However, unlike case *A*, case *B* allows nonlinear interactions among the first

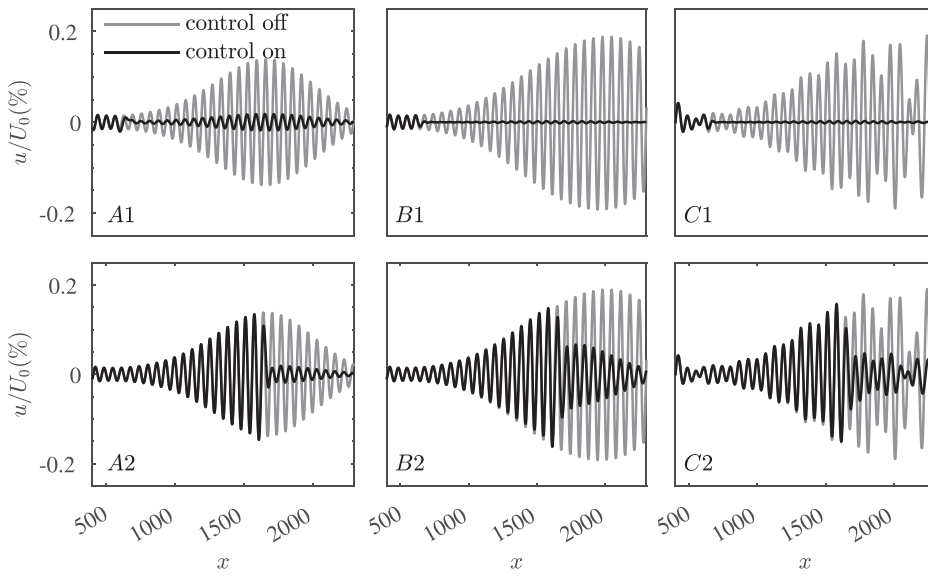


FIG. 5. Normalized maximum streamwise ( $u$ ) disturbance velocity, with and without control for control cases A – C.

TABLE III. Summary of test cases and TS wave's strength reduction (measured in decibels).

Cases	$\Delta u_{max}$ (dB)	$\Delta P_{err}$ (dB)
A1	-8.82	-8.91
A2	-8.37	-6.02
B1	-20.08	-15.13
B2	-4.93	-5.43
C1	-19.47	-11.95
C2	-6.47	-5.54
D1	-18.51	-11.64
D2	-5.36	-2.11

three harmonics of the TS wave and the mean flow distortion. Consequently, the second and third harmonics of the TS wave are naturally generated in the simulation domain through nonlinear interactions.

Similar to case A, the superior effectiveness of the upstream actuator remains evident in case B, as illustrated in Fig. 5. Unlike case A, the suppression of the TS wave through upstream actuation in case B is not local, and the remaining disturbances do not amplify rapidly beyond the actuator's location. This results in a suppression of 20 dB (99% reduction in TS amplitude) in case B1. However, the efficacy of the downstream actuator in case B2 is notably diminished resulting in a reduction of the TS amplitude by 5 dB (68%). The streamwise and wall-normal velocities and pressure fields are depicted in Fig. 6 for the nonlinear single-frequency case B2.

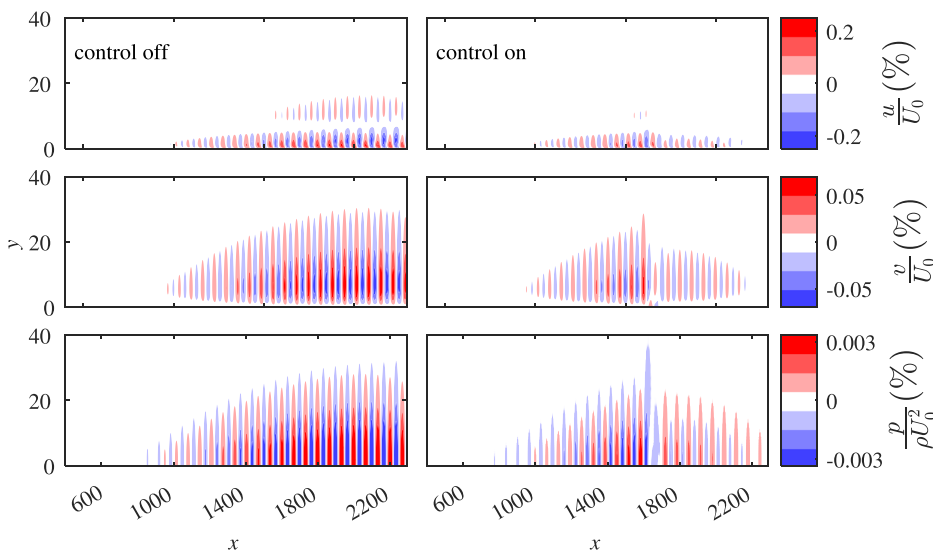


FIG. 6. Contours of normalized streamwise ( $u$ ), wall-normal ( $v$ ) disturbance velocity, and pressure ( $p$ ) for the nonlinear single-frequency case B2 (downstream control). The actuator is located at  $x = 1653$ .

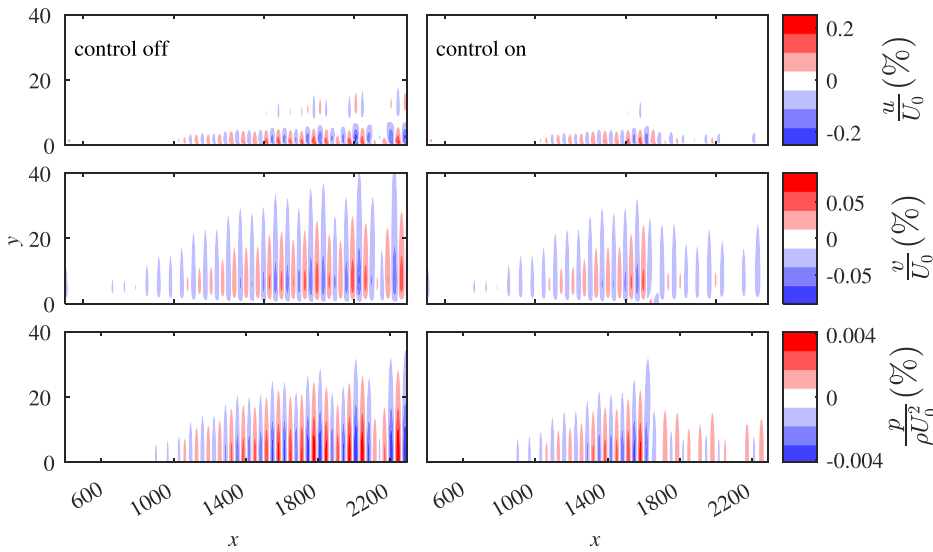


FIG. 7. Contours of normalized streamwise ( $u$ ), wall-normal ( $v$ ) disturbance velocity, and pressure ( $p$ ) with (right plots) and without (left plots) control for the nonlinear multi-frequency case C2 (downstream control), the actuator is located at  $x = 1653$ .

**C. Control cases C and D: Nonlinear multi-frequency control**

Moving beyond the investigation of the weakly nonlinear case B, this study explores the framework performance in nonlinear multi-frequency control cases. In case C, a wave train consisting of three TS modes ( $F = 86, 57$ , and  $28$ ) is initiated at the inflow. All modes are assigned equal initial amplitudes, as detailed in Sec. II A 1. The uncontrolled instability’s velocity and pressure perturbations, as depicted in Figs. 5 and 7, become more similar to naturally occurring TS waves when multiple modes are considered for the convective instability.

The nonlinear multi-frequency control case C is controlled using the superposition method, similar to case B. Despite dealing with a more complex ensemble of instabilities, the controller’s performance remains robust, leading to pressure perturbation attenuation of 12 dB for upstream control and 5.5 dB for downstream control in case C.

The effectiveness of the control system is further studied in test case D, wherein the initial amplitude of two modes is increased to intensify nonlinear interactions. In relation to case C, the initial amplitude of two modes ( $F = 28, 57$ ) is raised from 0.25% to 0.5%, while the amplitude of the third mode is maintained at 0.25%.

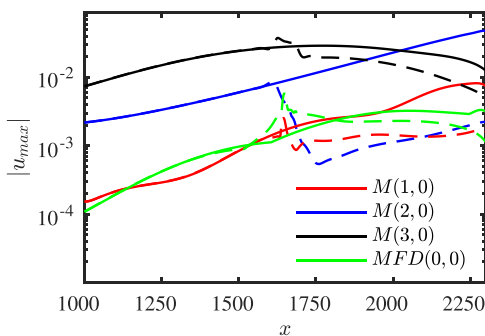


FIG. 8. Amplitude evolution of maximum streamwise ( $u_{max}$ ) disturbance velocity for the nonlinear multi-frequency case D2, control off (solid line), and control on (dashed line).

Figure 8 illustrates the modal amplitude evolution of the maximum streamwise velocity perturbation for controlled and uncontrolled case D2. The decrease in amplitude for the first and second modes is more pronounced than for the third mode. This observation follows the dominant influence of the most growing mode in this control scenario, exerting extra nonlinear forcing on the remaining modes. Consequently, controlling the dominant mode yields the most beneficial impact on other modes. In addition to the reduction in amplitude of the controlled instabilities, it is worth noting the growth rate reduction of the controlled waves downstream of the actuation, resulting in further attenuation of the waves.

It is apparent in Fig. 9 that a nearly complete wave cancellation is accomplished for case D1 when the actuator is positioned upstream.

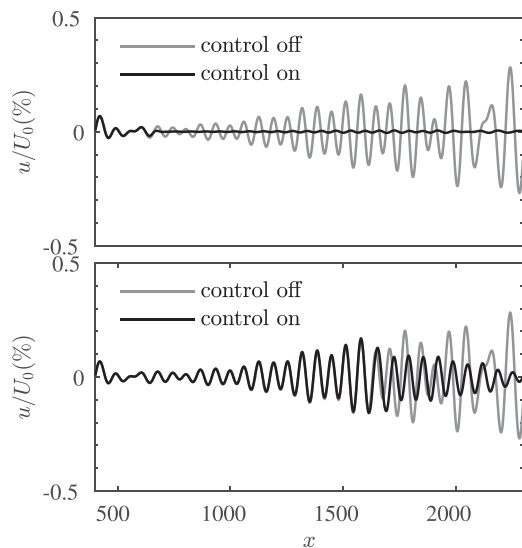
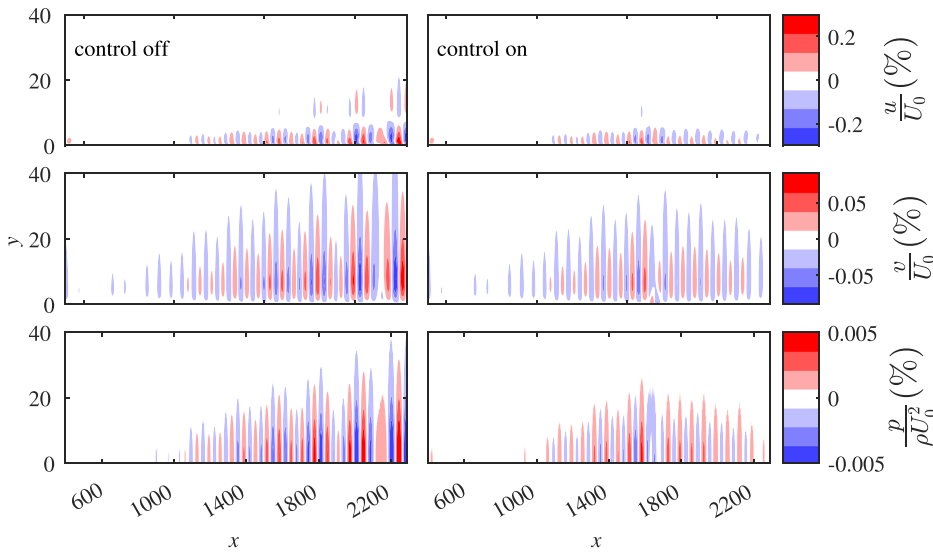


FIG. 9. Normalized maximum streamwise ( $u$ ) disturbance velocity, with and without control for the nonlinear multi-frequency: top: case D1 (upstream control), down: case D2 (downstream control).



**FIG. 10.** Contours of normalized streamwise ( $u$ ), wall-normal ( $v$ ) disturbance velocity, and pressure ( $p$ ) with (right plots) and without (left plots) control for the nonlinear multi-frequency case  $D2$  (downstream control), and actuator is located at  $x = 1653$ .

Despite lacking control authority over the spatial distribution and location of the jets, the controller effectively mitigates the incoming disturbances.

Although the attenuation of the disturbance signal is noticeable in case  $D2$ , as shown in Figs. 9 and 10, the effectiveness of the control system deteriorates when the actuator is located downstream. This is attributed to the characteristics of the superposition technique, which addresses each instability harmonic within a linear development framework. For instance, in case  $D2$ , the degree of dominance of nonlinear interactions escalates downstream due to the elevated initial amplitude of disturbances at the inflow. Consequently, the main assumption of the superposition method regarding the linear progress of the TS wave becomes invalid resulting in the deterioration of the control system’s effectiveness. The present study examined a limited set of nonlinear cases to establish proof of concept for the PSO controller across various scenarios. Further studies with more nonlinear control cases are required to precisely determine the threshold of applicability for the superposition methodology.

The results in the strongly nonlinear case  $D$  additionally offer insights in the workings of the superposition method. The plot in Fig. 11(a) illustrates the normalized streamwise velocity field when influenced solely by the upstream disturbance input, as seen in the uncontrolled scenario. Figure 11(b) depicts the velocity field when exclusively driven by the corresponding control input. The controlled case is also presented in Fig. 11(c). Comparing the plots in this figure demonstrates that the wave generated by the actuator shares an equal amplitude but opposite phase with the uncontrolled waves, resembling the opposition control strategy.

#### D. Discussion

A summary of all considered test cases with corresponding TS strength reduction with respect to the corresponding baseline (i.e., uncontrolled) case is presented in Table III. Here,  $\Delta u_{max}$  represents the maximum streamwise velocity reduction, while  $\Delta P_{err}$  signifies the reduction in pressure (error) signal as detected by the output sensor.

As evident in Table III, the controller’s performance is notably influenced by the actuator’s spatial placement within the simulation domain, as highlighted by the contrast between the cases 1 and 2. Moving the actuator downstream leads to a decrease in controller performance across all nonlinear test cases although the controller remains effective with more than 4.9 dB reduction in maximum instability amplitude.

In contrast, the suppression of TS waves for linear single-frequency (case  $A$ ) is not noticeably different by comparing cases  $A1$  and  $A2$ . This observation confirms that the performance deterioration of the controller downstream occurs exclusively in nonlinear cases where the assumption of linear progress of TS wave becomes invalid.

The noticeable difference between controller performance in cases  $A1$  and  $B1$  arises from different feedback observed by the error sensor always located at the same fixed location ( $X_{so} = 1782$ ). Specifically, the nonlinear interactions active in case  $B1$  will be

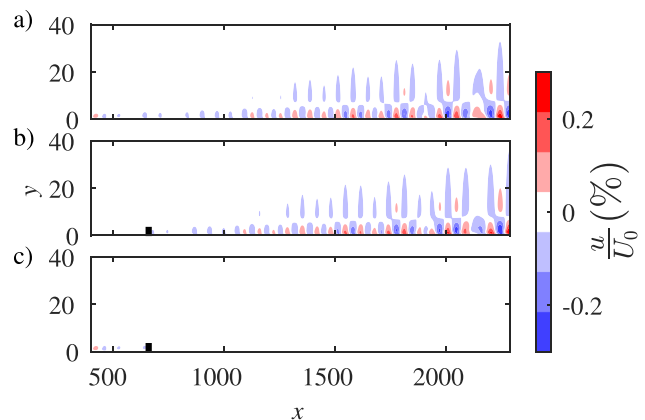


**FIG. 11.** Contours of normalized streamwise ( $u$ ) disturbance velocity for the nonlinear multi-frequency case  $D1$ . (a) (actuator off, input disturbance: on), (b) (actuator on, input disturbance: off), and (c) (actuator on, input disturbance: on), and actuator is indicated with a small black square.

registered in the feedback line of the controller. As shown in Fig. 5, the growth of the controlled TS waves after the actuator is the main source of differences between controller performance in cases A1 and B1. Therefore, the detection of the nonlinear interactions between different harmonics by the error sensor appears to aid the controller suppress these nonlinear interactions and delay the growth of controlled TS waves, while this information does not exist in the linear control case A. Although the amplitude of the higher harmonics in case B1 is still relatively small, the high sensitivity of the flow problem to minor changes can result in significant variations in the developed flow and the associated flow control problem. This effect is evident in Fig. 5, where even the uncontrolled flows in cases A1 and B1 exhibit noticeable differences downstream.

The lower control performance in case B2 compared to other test cases can be attributed to the scenario where the single-frequency TS wave introduced at the inflow transforms into a multi-frequency wave downstream, characterized by unknown (to the controller) amplitudes for the generated modes. This multi-frequency nature is not effectively captured by the input sensor, subsequently resulting in diminished controller performance downstream. This is further evident in the uncontrolled amplitude evolution for each case (Fig. 3), where the distinction of the higher harmonics is clearly more evident for the reference sensor in cases C and D compared to case B.

The controller’s performance in nonlinear multi-frequency control (case D) is presented in Table IV, indicating the suppression of each harmonic mode and mean flow distortion. The term  $\delta_A$  in Table IV is calculated by subtracting the amplitude reduction of each controlled mode from the amplitude reduction of that mode in a linear single-frequency control case. Examining the values of  $\delta_A$  for case D2 in Table IV, the reduced performance of the controller downstream is attributed to the challenge of attenuating the higher harmonic modes, which are more prone to nonlinear interactions developing downstream.

### E. Nonlinear controller design

Approaching the four considered control cases using the superposition method reveals a limitation in effectively suppressing

TABLE IV. TS wave’s modes strength reduction for multi-frequency nonlinear test cases.

Cases	Modes	$\Delta u_{max}$ (%)	$\delta_A$ (%)
D1	$M(1, 0)$	99, 93	7,4
	$M(2, 0)$	98, 67	0,81
	$M(3, 0)$	95, 30	-3,1
	$MFD(0, 0)$	99, 61	...
D2	$M(1, 0)$	83, 33	-9,31
	$M(2, 0)$	75, 36	-18,64
	$M(3, 0)$	68, 33	-17,65
	$MFD(0, 0)$	72, 96	...

nonlinearly developing TS waves at a late growth regime. To ascertain whether this limitation originated from the control method itself or is inherent to the PSO algorithm, a further control case is studied by considering a fully nonlinear design of the controller for case D2. This enables a performance comparison between a linearly designed controller using the superposition method (D2) and a nonlinearly designed one (D2n).

The nonlinearly designed controller effectively mitigates the high-amplitude TS wave downstream of the actuator, resulting in a reduction of 14.5 dB in maximum instability amplitude. This is notably superior to the 5 dB reduction achieved by the linearly designed controller in case D2. This is highlighted in Figs. 12 and 13, where the near-complete elimination of the instability waves is observable. The controller based on the superposition method lacks knowledge of the nonlinear harmonic mode interactions, leading to diminished performance in downstream control scenarios. This aligns with the suppression of harmonic modes presented in Table V, where the nonlinearly designed controller (D2n) has stronger attenuation of all modes, including mean flow distortion.

This approach overcomes the limitation of the superposition method in suppressing nonlinearly interacting modes, as can be seen

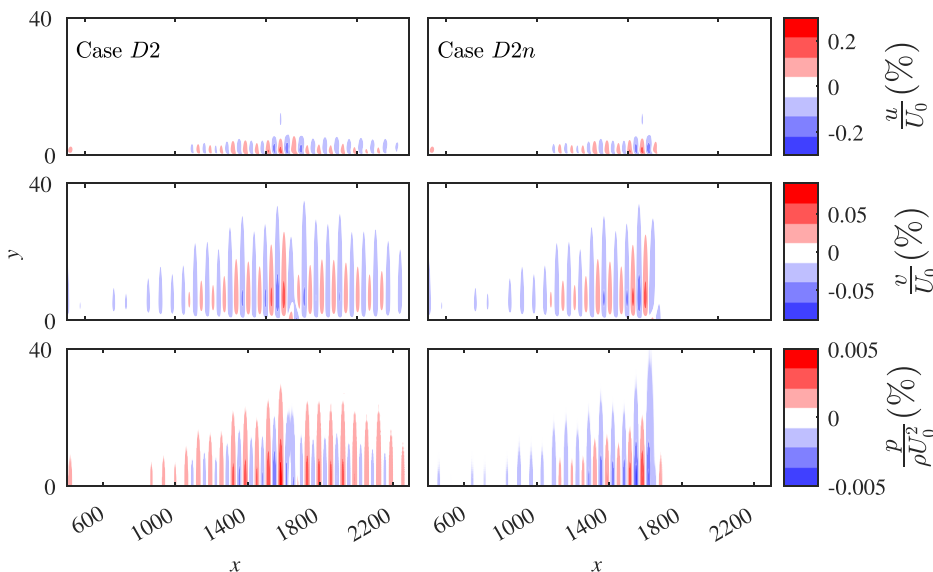
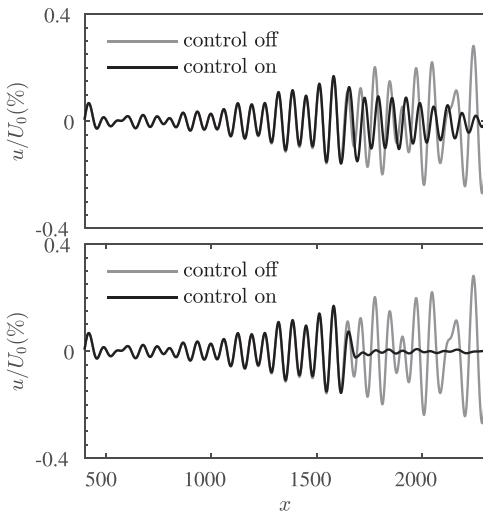


FIG. 12. Contours of normalized stream-wise ( $u$ ), wall-normal ( $v$ ) disturbance velocity, and pressure ( $p$ ) for the nonlinear multi-frequency case. Left: D2—linearly designed controller (superposition method); right: D2n—nonlinearly designed controller.



**FIG. 13.** Normalized maximum streamwise( $u$ ) disturbance velocity for the nonlinear multi-frequency case  $D2$ . Top: linearly designed controller (superposition method), down: nonlinearly designed controller.

in Fig. 14. Notably, this is achieved to an extent where the attenuation surpasses what can be attained through separate control of modes within a linear framework, as indicated by the positive  $\delta_A$  values for case  $D2n$  in Table V. This indicates that control of each harmonic mode positively influences the control of other harmonic modes within the nonlinearly designed controller by mitigating nonlinear interactions between controlled modes.

Comparing TS modal amplitude evolution in Fig. 14 for both linearly and nonlinearly designed controllers along with the uncontrolled case clarifies the performance difference in these two design approaches. The controllers effectively reduce the growth rate of modes  $(1, 0)$  and  $(3, 0)$ , concurrently decreasing the amplitude of the second mode without inducing any alterations to its growth rate. The amplitude of higher modes is rapidly attenuated in the nonlinear control method compared to the superposition method. The difference in TS suppression between the superposition method and the nonlinearly designed controller increases with higher frequency harmonic modes, as illustrated in Fig. 14 and Table V. The stronger effect of nonlinear interactions

**TABLE V.** TS wave's modes strength reduction for multi-frequency nonlinear test case  $D2$ , with ( $D2$ ) and without ( $D2n$ ) the superposition method.

Cases	Modes	$\Delta u_{max}$ (%)	$\delta_A$ (%)
$D2$	$M(1, 0)$	83.33	-9.31
	$M(2, 0)$	75.36	-18.64
	$M(3, 0)$	68.33	-17.65
	$MFD(0, 0)$	72.96	...
$D2n$	$M(1, 0)$	86.43	-6.21
	$M(2, 0)$	98.89	4.89
	$M(3, 0)$	95.07	9.09
	$MFD(0, 0)$	85.34	...

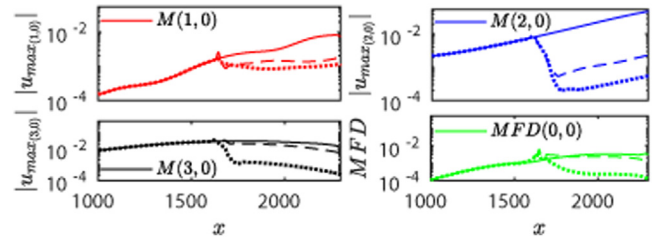


**FIG. 14.** Amplitude evolution of streamwise ( $u$ ) disturbance velocity for the nonlinear multi-frequency case  $D2$ , control off (solid line), and control on—linearly designed (dashed line) and nonlinearly designed (dotted line).  $(i, 0)$  refers to the  $i$ th mode of TS wave and so on.

on higher frequency harmonic modes explains this observation making those modes more prone to nonlinear effects.

#### IV. CONCLUSION

In the present work, a PSO-based controller for active control of Tollmien–Schlichting waves is introduced and studied numerically. The numerical framework solves the harmonic two-dimensional Navier–Stokes equations for zero pressure gradient boundary layer based on perturbation formulation and harmonic balancing. A closed-loop feedforward control system is utilized, consisting of wall-mounted harmonic suction and blowing jets as actuators controlled by the PSO algorithm to ascertain the optimal amplitude and phase for maximum wave suppression. The integration of this AI-based algorithm into the controller design process has proven highly effective in realizing the suppression of TS waves through an opposition control strategy.

Several test cases of single and multi-frequency TS control cases are explored to study the performance of the controller in various linear and nonlinear stages of TS wave development. TS wave attenuation is observed in all test cases, with an 8.5 dB (86%) reduction in the maximum amplitude of instabilities for linear single-frequency test cases and a reduction of up to 20 dB (99%) for nonlinear multi-frequency control cases. Delving into nonlinear multi-frequency control cases, two design approaches are followed, namely, linear superposition and nonlinear controller design.

A notable performance deterioration in downstream control scenarios has been identified for the linearly designed controller, stemming from amplified nonlinear interactions between higher-frequency modes that deviate from the linear TS wave approximation in the superposition method. This highlights the limitation of linear approaches in detecting and controlling complex nonlinear interactions. In contrast, the nonlinearly designed controller demonstrates effective performance in mitigating nonlinear multi-frequency instabilities at late growth regimes. This controller exhibits a reduction of 14.5 dB in maximum instability amplitude, indicative of near-complete instability wave elimination, thus proving the ability of the PSO-based harmonic suction and blowing jets to suppress naturally occurring Tollmien–Schlichting waves in their nonlinear growth regime.

This study exhibits the capability of AI-based control strategies to extend the active control of convective instabilities beyond the linear growth regime. This improves sensor detection capabilities for disturbances and extends the temporal and spatial control horizon into the nonlinear growth regime, thereby enhancing flexibility in positioning

and broadening the range of actuators and sensors applicable in future control systems.

Future research could explore alternative AI-based algorithms, especially Machine Learning (ML) techniques like Deep Reinforcement Learning (DRL). These approaches, which utilize Neural Networks, are expected to have a better performance for control of convective instabilities in nonlinear growth regimes.

## AUTHOR DECLARATIONS

### Conflict of Interest

The authors have no conflicts to disclose.

## Author Contributions

**B. Mohammadikalakoo:** Conceptualization (equal); Formal analysis (equal); Investigation (equal); Methodology (equal); Validation (equal); Visualization (equal); Writing – original draft (equal). **M. Kotsonis:** Conceptualization (equal); Formal analysis (equal); Methodology (equal); Project administration (equal); Supervision (equal); Writing – review & editing (equal). **N. A. K. Doan:** Conceptualization (equal); Formal analysis (equal); Methodology (equal); Project administration (equal); Supervision (equal); Writing – review & editing (equal).

## DATA AVAILABILITY

The data that support the findings of this study are available from the corresponding author upon reasonable request.

## REFERENCES

- <sup>1</sup>S. Bagheri and D. S. Henningson, “Transition delay using control theory,” *Philos. Trans. R. Soc. A* **369**, 1365–1381 (2011).
- <sup>2</sup>A. S. Thomas, “The control of boundary-layer transition using a wave-superposition principle,” *J. Fluid Mech.* **137**, 233 (1983).
- <sup>3</sup>L. B. Cossu, “Stabilization of Tollmien-Schlichting waves by finite amplitude optimal streaks in the Blasius boundary layer,” *Phys. Fluids* **14**, L57 (2002).
- <sup>4</sup>M. Kotsonis, R. Giepmans, S. Hulshoff, and L. Veldhuis, “Numerical study of the control of Tollmien-Schlichting waves using plasma actuators,” *AIAA J.* **51**, 2353–2364 (2013).
- <sup>5</sup>T. Michelis, A. B. Putranto, and M. Kotsonis, “Attenuation of Tollmien-Schlichting waves using resonating surface-embedded phononic crystals,” *Phys. Fluids* **35**, 044101 (2023).
- <sup>6</sup>R. Milling, “Tollmien-Schlichting wave cancellation,” *Phys. Fluids* **24**, 979 (1981).
- <sup>7</sup>H. W. Liepmann, G. L. Brown, and D. M. Nosenchuck, “Control of laminar-instability waves using a new technique,” *J. Fluid Mech.* **118**, 187–200 (1982).
- <sup>8</sup>R. D. Joslin, “Validation of three-dimensional incompressible spatial direct numerical simulation code: A comparison with linear stability and parabolic stability equation theories for boundary-layer transition on a flat plate,” Technical Publication (TP) (National Aeronautics and Space Administration, Office of Management, Scientific and Technical Information Program, 1992).
- <sup>9</sup>O. Semeraro, S. Bagheri, L. Brandt, and D. S. Henningson, “Transition delay in a boundary layer flow using active control,” *J. Fluid Mech.* **731**, 288–311 (2013).
- <sup>10</sup>H. J. Tol, C. C. de Visser, and M. Kotsonis, “Experimental model-based estimation and control of natural Tollmien-Schlichting waves,” *AIAA J.* **57**, 2344–2355 (2019).
- <sup>11</sup>D. J. Sturzebecher and W. H. Nitsche, “Active cancellation of Tollmien-Schlichting instabilities on a wing using multi-channel sensor actuator systems,” *Int. J. Heat Fluid Flow* **24**, 572–583 (2003).
- <sup>12</sup>A. Kurz, N. Goldin, R. King, C. Tropea, and S. Grundmann, “Hybrid transition control approach for plasma actuators,” *Exp. Fluids* **54**, 1–4 (2013).
- <sup>13</sup>M. Kotsonis, R. K. Shukla, and S. Pröbsting, “Control of natural Tollmien-Schlichting waves using dielectric barrier discharge plasma actuators,” *Int. J. Flow Control* **7**, 37–54 (2015).
- <sup>14</sup>B. Simon, N. Fabbiane, T. Nemitz *et al.*, “In-flight active wave cancellation with delayed-x-LMS control algorithm in a laminar boundary layer,” *Exp. Fluids* **57**, 160 (2016).
- <sup>15</sup>D. B. S. Audiffred, A. V. G. Cavalieri, P. P. C. Brito, and E. Martini, “Experimental control of Tollmien-Schlichting waves using the Wiener-Hopf formalism,” *Phys. Rev. Fluids* **8**, 073902 (2023).
- <sup>16</sup>B. A. Belson, O. Semeraro, C. W. Rowley, and D. S. Henningson, “Feedback control of instabilities in the two-dimensional Blasius boundary layer: The role of sensors and actuators,” *Phys. Fluids* **25**, 054106 (2013).
- <sup>17</sup>H. J. Tol, M. Kotsonis, C. C. D. Visser, and B. Bamieh, “Localised estimation and control of linear instabilities in two-dimensional wall-bounded shear flows,” *J. Fluid Mech.* **824**, 818–865 (2017).
- <sup>18</sup>D. Ladd and E. Hendricks, “Active control of 2-D instability waves on an axisymmetric body,” *Exp. Fluids* **6**, 69–70 (1988).
- <sup>19</sup>P. Pupator and W. Saric, “Control of random disturbances in a laminar boundary layer,” in *AIAA 2nd Shear Flow Conference* (1989).
- <sup>20</sup>D. Ladd, “Control of natural instability waves on an axisymmetric body,” *AIAA J.* **28**, 367–369 (1990).
- <sup>21</sup>M. Baumann and W. Nitsche, “Investigation of active control of Tollmien-Schlichting waves on a wing,” in *Transitional Boundary Layers in Aeronautics*, edited by R. Henkes and J. van Ingen (KNAW, Amsterdam, Netherlands, 1996), Vol. 46, pp. 89–98.
- <sup>22</sup>M. Baumann and W. Nitsche, “Experiments on active control of Tollmien-Schlichting waves on a wing,” in *New Results in Numerical and Experimental Fluid Mechanics: Contributions to the 10th AG STAB/DGLR Symposium Braunschweig, Germany 1996*, edited by H. Körner and R. Hilbig (Vieweg+Teubner Verlag, Wiesbaden, 1997), pp. 56–63.
- <sup>23</sup>M. Baumann, D. Sturzebecher, and W. Nitsche, “Active control of TS-instabilities on an unswept wing,” in *Laminar-Turbulent Transition, IUTAM Symposium Sedona/AZ 1999*, edited by H. Fasel and W. Saric (Springer-Verlag, 2000), pp. 155–160.
- <sup>24</sup>F. Ren, H. b Hu, and H. Tang, “Active flow control using machine learning: A brief review,” *J. Hydrodyn.* **32**, 247–253 (2020).
- <sup>25</sup>S. H. Rudy, S. L. Brunton, J. L. Proctor, and J. N. Kutz, “Data-driven discovery of partial differential equations,” *Sci. Adv.* **3**, e1602614 (2017).
- <sup>26</sup>L. Zhu, W. Zhang, J. Kou, and Y. Liu, “Machine learning methods for turbulence modeling in subsonic flows around airfoils,” *Phys. Fluids* **31**, 015105 (2019).
- <sup>27</sup>J. Li, M. Zhang, J. R. Martins, and C. Shu, “Efficient aerodynamic shape optimization with deep-learning-based geometric filtering,” *AIAA J.* **58**, 4243–4259 (2020).
- <sup>28</sup>J. Li and M. Zhang, “Adjoint-free aerodynamic shape optimization of the common research model wing,” *AIAA J.* **59**, 1–11 (2021).
- <sup>29</sup>S. Sun, S. Liu, J. Liu, and H. I. Schlaberg, “Wind field reconstruction using inverse process with optimal sensor placement,” *IEEE Trans. Sustainable Energy* **10**, 1290–1299 (2019).
- <sup>30</sup>J. Rabault, M. Kuchta, A. Jensen *et al.*, “Artificial neural networks trained through deep reinforcement learning discover control strategies for active flow control,” *J. Fluid Mech.* **865**, 281–302 (2019).
- <sup>31</sup>J. Rabault and A. Kuhnle, “Accelerating deep reinforcement learning strategies of flow control through a multi-environment approach,” *Phys. Fluids* **31**, 094105 (2019).
- <sup>32</sup>J. Li and M. Zhang, “Reinforcement-learning-based control of confined cylinder wakes with stability analyses,” *J. Fluid Mech.* **932**, A44 (2022).
- <sup>33</sup>W. Chen, Q. Wang, L. Yan, G. Hu, and B. R. Noack, “Deep reinforcement learning-based active flow control of vortex-induced vibration of a square cylinder,” *Phys. Fluids* **35**, 053610 (2023).
- <sup>34</sup>C. Wang, P. Yu, and H. Huang, “Reinforcement-learning-based parameter optimization of a splitter plate downstream in cylinder wake with stability analyses,” *Phys. Rev. Fluids* **8**, 083904 (2023).
- <sup>35</sup>B. Mohammadikalakoo, M. Kotsonis, and N. A. K. Doan, “Optimization of Tollmien-Schlichting waves control: Comparison between deep reinforcement learning and particle swarm optimization approach,” in *13th International Symposium on Turbulence and Shear Flow Phenomena (TSFP13)*, Montréal, Canada (2024).
- <sup>36</sup>B. Mohammadikalakoo, M. Kotsonis, and N. A. K. Doan, “Real-time control of Tollmien Schlichting waves with single-step deep reinforcement learning,” in *IUTAM Symposium on Laminar-Turbulent Transition*, Nagano, Japan (2024).



- <sup>37</sup>F. Ren, J. Rabault, and H. Tang, "Applying deep reinforcement learning to active flow control in weakly turbulent conditions," *Phys. Fluids* **33**, 037121 (2021).
- <sup>38</sup>L. Guastoni, J. Rabault, P. Schlatter, H. Azizpour, and R. Vinuesa, "Deep reinforcement learning for turbulent drag reduction in channel flows," *Eur. Phys. J. E* **46**, 27 (2023).
- <sup>39</sup>J. Kennedy and R. Eberhart, "Particle swarm optimization," in *Proceedings of ICNN'95 - International Conference on Neural Networks* (IEEE, 1995), Vol. 4, pp. 1942–1948.
- <sup>40</sup>Z. Wenjing, "Parameter identification of Lugre friction model in servo system based on improved particle swarm optimization algorithm," in *Chinese Control Conference* (IEEE, 2007), pp. 135–139.
- <sup>41</sup>C.-C. Hung, and L. Wan, "Hybridization of particle swarm optimization with the k-means algorithm for image classification," in *IEEE Symposium on Computational Intelligence for Image Processing* (IEEE, 2009), pp. 60–64.
- <sup>42</sup>Q. Bai, "Analysis of particle swarm optimization algorithm," *Comput. Inf. Sci.* **3**, 180–184 (2010).
- <sup>43</sup>K. Premalatha and A. M. Natarajan, "Hybrid PSO and GA for global maximization," *Int. J. Open Probl. Compt. Math* **2**, 597–608 (2009); available at [https://www.researchgate.net/publication/267239415\\_Hybrid\\_PSO\\_and\\_GA\\_for\\_global\\_maximization](https://www.researchgate.net/publication/267239415_Hybrid_PSO_and_GA_for_global_maximization).
- <sup>44</sup>E. di Mario, Z. Talebpour, and A. Martinoli, "A comparison of PSO and Reinforcement Learning for multi-robot obstacle avoidance," in *2013 IEEE Congress on Evolutionary Computation* (IEEE, 2013), pp. 149–156.
- <sup>45</sup>P. Moravec and P. Rudolf, "Application of a particle swarm optimization for shape optimization in hydraulic machinery," *EPJ Web Conf.* **143**, 02076 (2017).
- <sup>46</sup>B. Torner, D. Frank, S. Grundmann, and F. H. Wurm, "Flow simulation-based particle swarm optimization for developing improved hemolysis models," *Biomech. Model. Mechanobiol.* **22**, 401–416 (2023).
- <sup>47</sup>S. Westerbeek, S. Hulshoff, H. Schuttelaars, and M. Kotsonis, "DeHNSSo: The Delft Harmonic Navier-Stokes Solver for nonlinear stability problems with complex geometric features," *Comput. Phys. Commun.* **302**, 109250 (2024).
- <sup>48</sup>F. Bertolotti, T. Herbert, and P. Spalart, "Linear and nonlinear stability of the Blasius boundary layer," *J. Fluid Mech.* **242**, 441–474 (1992).
- <sup>49</sup>T. Herbert, "Special course on progress in transition modelling," *J. AGARD* R793 5 (1994).
- <sup>50</sup>M. R. Malik, "Numerical methods for hypersonic boundary layer stability," *J. Comput. Phys.* **86**, 376–413 (1990).
- <sup>51</sup>C. Streeb and M. Macaraeg, "Spectral multi-domain for large-scale fluid dynamic simulations," *Appl. Numer. Math.* **6**, 123–139 (1989).
- <sup>52</sup>C. Hall, J. P. Thomas, and W. S. Clark, "Computation of unsteady nonlinear flows in cascades using a harmonic balance technique," *AIAA J.* **40**, 879–886 (2002).
- <sup>53</sup>Y. Li and Y. Zhang, "Hyper-parameter estimation method with particle swarm optimization," *arXiv:2011.11944v2* [cs.LG] (2020).
- <sup>54</sup>Y. H. Shi and R. Eberhart, "A modified Particle Swarm Optimizer," in *Proceedings of the IEEE International Conference on Evolutionary Computation (ICEC)* (IEEE, 1998), pp. 69–73.
- <sup>55</sup>M. Jiang, Y. P. Luo, and S. Y. Yang, "Stochastic convergence analysis and parameter selection of the standard particle swarm optimization algorithm," *Inf. Process. Lett.* **102**, 8–16 (2007).